Journal of Materials Chemistry A

ROYAL SOCIETY OF CHEMISTRY

PAPER

View Article Online
View Journal | View Issue

Check for updates

Cite this: *J. Mater. Chem. A*, 2025, **13**, 10622

Advanced interfacial charge carrier transport enabling the improvement of open-circuit voltage in Sb_2Se_3 solar cells†

Geumha Lim,‡[a] Van-Quy Hoang,‡[b] Jaebaek Lee,[b] Jin-Kyu Kang,[b] Kee-Jeong Yang,[b] Shi-Joon Sung,*[b] Dae-Hwan Kim*[b] and William Jo*[a]

Received 24th January 2025
Accepted 4th March 2025

DOI: 10.1039/d5ta00683j

rsc.li/materials-a

Effective charge carrier flow is essential for optimizing the optoelectrical properties of antimony selenide (Sb_2Se_3) and achieving highly efficient solar cells. $MoSe_2$, as an interlayer between Sb_2Se_3 and an Mo back-contact layer, serves as a seed layer for the preferential growth of Sb_2Se_3 nanorod structures, facilitating efficient electron transfer. This study focuses on investigating the altered electrical properties at the surface and interfaces of Sb_2Se_3, highlighting the previously unexplored influence of $MoSe_2$ on the interfacial carrier transport mechanism. Through the introduction of $MoSe_2$, a well grown Sb_2Se_3 rod array with a (*hk*1) orientation was achieved, along with a notable increase in vertical current flow. By exposing the back interface using a dimple-grinder, the direct examination of the interface band alignment revealed the role of $MoSe_2$ as an electron barrier. These effects led to a 95% improvement in power conversion efficiency (PCE), along with significant enhancements in open-circuit voltage (V_{OC}) and fill factor (FF), underscoring the importance of optimizing interface contact quality.

Introduction

Antimony selenide (Sb_2Se_3) has recently emerged as a next-generation light-absorbing material with promising optoelectronic properties for photovoltaic applications.[1] Its intrinsic features, such as benign grain boundaries without dangling bonds, were expected to result in high power conversion efficiency.[2] However, despite extensive efforts, the performance of Sb_2Se_3 solar cells remains below expectations.

One critical strategy for enhancing the photovoltaic performance of Sb_2Se_3 involves modulating its anisotropic charge carrier transport behavior.[3] In its unique one-dimensional nano-ribbon structure, charge carriers can flow efficiently in the [001] direction along the ribbons. In contrast, along the [100] direction where nano-ribbons are connected *via* weak van der Waals forces, electron transport becomes challenging as carriers must hop across the gaps.[4] Various approaches to achieve preferential grain growth of Sb_2Se_3 have been investigated, revealing that substrate selection plays a key role in controlling crystal growth orientation.[5,6] Many materials have been introduced to enhance the optical and electrical properties of the absorber layer in substrate-configured Sb_2Se_3 solar cells. For instance, Zhang reported a buried Se seed layer to create a Se-rich environment, reducing selenium vacancies (V_{Se}), antimony on selenium sites (Sb_{Se}), and interface defects.[7] In addition, a high-resistivity AlO_x layer was used as a passivation layer to enhance device efficiency by inhibiting recombination at the ITO/Sb_2Se_3 interface.[8] Rijal reported a champion PCE of 7.47% for substrate-type Sb_2Se_3 solar cells by using an Sb_2Se_3 seed layer to optimize grain orientation, crystallinity, and rear-interface properties.[9] In particular, in Sb_2Se_3 solar cells with an Mo substrate, the introduction of an $MoSe_2$ seed layer facilitates the formation of an Sb_2Se_3 nanorod structure with (*hk*1) orientation. This occurs because $MoSe_2$ provides a localized distribution of high surface-energy planes.[10] As a consequence, vertically grown Sb_2Se_3 enables efficient carrier transport along the rod structure, contributing to improved device efficiency.[11] In addition to the structural modifications, changes in the interfacial electrical properties were also expected; however, direct investigations into these effects have been limited. Establishing a well-defined interface between Sb_2Se_3 and Mo can enhance hole extraction, thereby improving the open-circuit voltage.[12,13] In this context, incorporating interlayers such as $MoSe_2$ can substantially influence interfacial electrical properties. In the case of CIGS or kesterite, studies report differing views on the benefits of band structure changes induced by $MoSe_2$.[14–16] To resolve this ambiguity, direct characterization of interfacial contact properties is essential.

[a]*Department of Physics, Ewha Womans University, Seoul, 03760, Republic of Korea. E-mail: wmjo@ewha.ac.kr*

[b]*Division of Energy & Environmental Technology, Daegu Gyeongbuk Institute of Science and Technology (DGIST), Daegu, 42988, Republic of Korea. E-mail: sjsung@dgist.ac.kr; monolith@dgist.ac.kr*

† Electronic supplementary information (ESI) available. See DOI: https://doi.org/10.1039/d5ta00683j

‡ Geumha Lim and Van-Quy Hoang equally contributed to this work.

The current study primarily aimed to unveil the carrier flow dynamics of Sb_2Se_3 and its interface with the back contact layer. Among the various deposition methods, co-evaporation was employed owing to its high reproducibility and suitability for large-area applications, although its relatively low record efficiency warrants further investigation. By modifying the back interface of Mo/Sb_2Se_3 with an $MoSe_2$ interlayer, structural modification and efficiency improvement were achieved. $MoSe_2$ facilitated the formation of (*hk*1)-oriented Sb_2Se_3 nanorod films, which enhanced charge carrier flow and reduced carrier recombination at grain boundaries. The vertical carrier path throughout the device was identified by analyzing the current flow within the absorber. Cross-sectional band alignment was directly characterized using potential distribution measured at the laterally exposed interface through dimple grinding.[17] The results revealed that $MoSe_2$ creates an energy barrier for electrons, effectively blocking electrons while promoting hole transport. Consequently, improved back contact quality reduces interfacial charge recombination, enhancing charge carrier collection, and thereby optimizing the open-circuit voltage.

Experimental method

Fabrication

Ultrathin $MoSe_2$ layer. The Mo back electrode was sputtered (DC) onto SLG substrates. An ultrathin $MoSe_2$ layer (~5 nm) was deposited at T_{sub} = 600 °C, followed by a lower-temperature growth step at T_{source} = 630 °C and T_{sub} = 315 °C.

Fabrication of the Sb_2Se_3 device. The solar cells were processed in a stack of SLG/Mo/$MoSe_2$/Sb_2Se_3/SnO_x/CdS/*i*-ZnO/ZnO : Al. Reference Sb_2Se_3 samples were fabricated without the $MoSe_2$ layer, where the source tray was rapidly heated to T_{sub} = 315 °C without intentional Mo selenization of the substrate. A 50 nm CdS buffer layer was deposited using chemical bath deposition to complete the device. To prevent Sb diffusion into the CdS layer during the process, a 2 nm ultrathin SnO_x layer was deposited onto the absorber *via* ALD. The solar cell stacks were finalized by sputtering *i*-ZnO (50 nm) and ZnO : Al (300 nm) layers on top. Finally, all samples were sectioned into 16 solar cells (A = 0.185 cm^2) by scribing, as described in previous studies.

Characterization

Surface and cross-sectional images were obtained using a field-emission scanning electron microscope (FESEM; Hitachi S-4800). STEM-EDS was used for elemental mapping of the prepared materials. Raman spectra were obtained at room temperature (~25 °C) using a micro-Raman system in back-scattering geometry with a 532 nm excitation wavelength. The laser power was set to 1 mW to avoid beam damage. KPFM and c-AFM were performed using an atomic force microscope (MFP3D Origin, Oxford Instruments). A Pt/Ir-coated tip was used for KPFM to obtain the V_{CPD} map, while a Ti/Pt-coated tip was used for c-AFM to acquire local current maps. A dimple grinder (model 657, Gatan Inc.) was employed to expose the Sb_2Se_3/back-contact interface by grinding the devices for 10 min using a polishing wheel with a diameter of 15 mm. Raman spectra at the exposed interface were obtained with a Raman spectrometer (XPE-35, Nanobase Inc.) using a laser with a wavelength of 532 nm. The laser power was set to 1 mW to avoid beam damage. Current–voltage curves were recorded under a simulated air mass spectrum of 1.5 global (AM 1.5 G) and 100 mW cm^{-1-2} (1 sun) illumination using a 94022A solar simulator (Newport Co). External quantum efficiency (EQE) was measured with EQE equipment (McScience) equipped with a Xe lamp source. It is important to note that conversion efficiencies were determined without the application of an antireflection coating or post-deposition treatment.

Results and discussion

The top-view and cross-sectional SEM images displayed in Fig. 1a–d illustrate the morphological evolution of co-evaporated Sb_2Se_3 films grown on different substrates. It was found that introducing the $MoSe_2$ interlayer on the Mo substrate induced a transformation in the morphology of the Sb_2Se_3 films, from a uniform single-layer thin film to a hybrid double-layer structure comprising vertically aligned nanorod arrays on a densely packed bottom layer. This indicates that the thickness of Sb_2Se_3, with the 1D nanorods extruding to approximately 1 μm in length above the compact bottom layer, follows the growth mechanism of Sb_2Se_3 from surface absorption to the nanorod array growth stage.[11] In particular, the growth behavior of Sb_2Se_3 crystals is strongly influenced by the substrate type, evaporation rates of the sources, and substrate temperature. Based on our prior investigations, we meticulously evaluated the morphological evolution of co-evaporated Sb_2Se_3 thin films, transitioning from initially flat and uniform absorbers to intricately structured nanorod arrays, utilizing a substantial 100-nm thick $MoSe_2$ interlayer. The intricate nanostructure of Sb_2Se_3 nanorods enables efficient transport of photo-generated carriers from the absorber to the CdS buffer layer, yielding a high-quality, preferentially oriented (*hk*1) array of Sb_2Se_3 nanorods engineered for enhanced solar cell efficiency. Therefore, a continuous Sb_2Se_3 film formed on the ultrathin $MoSe_2$ interlayer was anticipated to aid in investigating the morphological and electrical properties of the flat, uniform regions of Sb_2Se_3 (Fig. S1a and c, ESI†). Fig. S1b and d† present the results of a histogram analysis of the grain size of the co-evaporated Sb_2Se_3 films on different substrates. The representative grain size of Sb_2Se_3 increases from 262 nm to 292 nm, accompanied by a higher void density, with the selenization of the Mo substrate. The morphological evolution of Sb_2Se_3 could be attributed to altered crystal growth mechanisms, due to the differences in surface energy and nucleation dynamics betweenSb_2Se_3 and the $MoSe_2$ interlayer. A larger grain size generally contributes to enhanced optoelectronic properties by reducing grain boundary density, which can lower non-radiative recombination and improve charge transport. The $MoSe_2$ interlayer plays a critical role in controlling the morphology of the Sb_2Se_3 thin films and their interfacial properties. The top 1D nanorod array layer potentially influences the interconnection between the Sb_2Se_3 absorber layer and n-type CdS layer. To

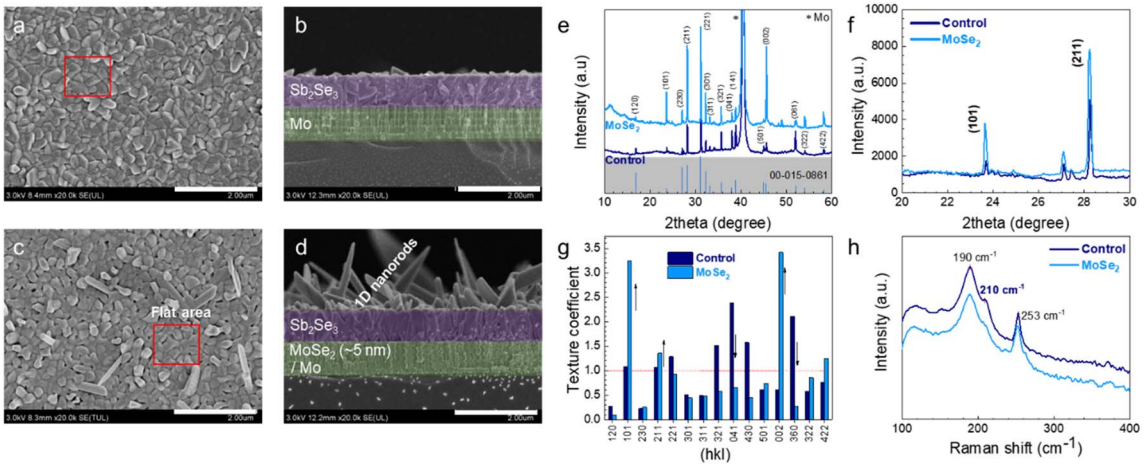

Fig. 1 Top-view and cross-sectional scanning electron microscopy (SEM) images of Sb_2Se_3 films deposited on (a and b) A(Mo) and (c and d) selenized Mo-coated glass B($MoSe_2$) under *in situ* co-evaporation conditions. (e) X-ray diffraction (XRD) patterns of co-evaporated Sb_2Se_3 films on A(Mo) and B($MoSe_2$), with the standard diffraction pattern (JCPDS 00-015-0861) included as a reference. (f) Enlarged XRD patterns, (g) corresponding calculated texture coefficients, and (h) Raman spectra of Sb_2Se_3 films deposited on A(Mo) or B($MoSe_2$) substrates.

mitigate Se loss and prevent Sb diffusion into CdS, which is triggered by the nanorod structure, the use of an ultrathin $MoSe_2$ interlayer is essential. Based on these findings, we conclude that optimizing the properties of $MoSe_2$ is crucial for developing Sb_2Se_3 nanorod-structured solar cells.

The XRD patterns of Sb_2Se_3 films without and with the $MoSe_2$ interlayer (Fig. 1e) display strong (*hk*1) diffraction peaks, apart from a high-intensity peak corresponding to the Mo substrate onto which the films were deposited. The peaks attributed to the absorber were indexed to the orthorhombic phase of Sb_2Se_3 without any detectable impurities, and the space group was *Pbnm* (62).[12,18,19] The Sb_2Se_3 film deposited on the $MoSe_2$ substrate exhibits better crystallinity than that on the bare Mo substrate, particularly at the typical peak positions of (101) and (221), as illustrated in the enlarged XRD patterns in Fig. 1f. It is widely accepted that in a film composed of [*hk*0]-oriented grains – (120), (230), (340), and (360) planes – the ribbons are stacked parallel to the Mo substrate. In contrast, a film composed of (*hk*1)-oriented grains contains ribbons that are arranged perpendicular to the substrate. By calculating the texture coefficients (TC) of these peaks, we identified the typical crystal planes of Sb_2Se_3 films. TC, a structural parameter defining the texture of a given plane, is expressed as follows:

$$\mathrm{TC}_{hkl} = \frac{I_{(hkl)}}{I_{0(hkl)}} \Bigg/ \left(\frac{1}{N} \sum_{N} \frac{I_{(hkl)}}{I_{0(hkl)}} \right), \quad (1)$$

where $I_{(hkl)}$ denotes the intensity of the experimentally measured (*hkl*) diffraction peak, $I_{0(hkl)}$ represents the intensity of the reflection reported in the JCPDS card, and N denotes the number of Miller indices considered in the analysis.

All Sb_2Se_3 films exhibited (*hk*1)-preferred orientations with the TC of the (*hk*1) planes of the Sb_2Se_3 films deposited onto $MoSe_2$ exceeding that of the Sb_2Se_3 films on bare Mo substrates (Fig. 1g). Given that $(Sb_4Se_6)_n$ ribbons are arranged perpendicular to the substrate and carriers are preferentially transported within the ribbons, the (*hk*1)-plane-dominated structure is more suitable for carrier transport in the Sb_2Se_3 absorber layer, leading to higher conductivity. In addition, the vertically aligned nanorods can improve light trapping, potentially increasing absorption. Raman scattering was employed to further examine the structures of Sb_2Se_3 films and their impurity phases on different substrates, as depicted in Fig. 1h. The vibrational mode at 190 cm^{-1} and the peak corresponding to the stretching vibrations of the Se–Se bond in Se chains and Se_8 rings at 253 cm^{-1} were observed in all the films, consistent with previously reported studies.[20] These bands did not exhibit significant changes upon Mo selenization treatments, indicating that the bulk structure of Sb_2Se_3 was not substantially affected.

To evaluate the photovoltaic characteristics of the co-evaporated Sb_2Se_3 thin films deposited onto Mo and $MoSe_2$/Mo substrates, Sb_2Se_3 solar cells with a substrate configuration structure of soda lime glass (SLG)/Mo/($MoSe_2$)/Sb_2Se_3/(SnO_x)/CdS/*i*-ZnO/AZO/Al were fabricated. The ALD_SnO_x layer was applied on top of the Sb_2Se_3 layer before CdS deposition to prevent Sb diffusion into the CdS layer, ensuring reproducibility. Fig. 2a and b illustrate the cross-sectional TEM and HAADF STEM images of the back Mo/Sb_2Se_3 and front Sb_2Se_3/CdS interfaces of Sb_2Se_3 solar cell devices A(Mo) and B($MoSe_2$). Notably, the Sb_2Se_3 solar cells exhibited a flat, planar structure in both configurations, with and without the ultrathin (5 nm) $MoSe_2$ interlayer, consistent with findings from our previous studies.[5,10] For B($MoSe_2$), the high-resolution STEM image confirmed an $MoSe_2$ interlayer thickness of approximately 5 nm, while for A (Mo), the corresponding image confirmed a smooth interface between the Mo and Sb_2Se_3 layers. According to the HAADF STEM images, the Sb_2Se_3 layer exhibits a dense structure comprising voids (empty volumes) and Sb_2Se_3 (filled volume). From the front contact, the CdS buffer, *i*-ZnO window, and TCO layers were uniformly deposited onto the flat Sb_2Se_3 absorber layer without any nanorod arrays. Fig. 2d–f present the

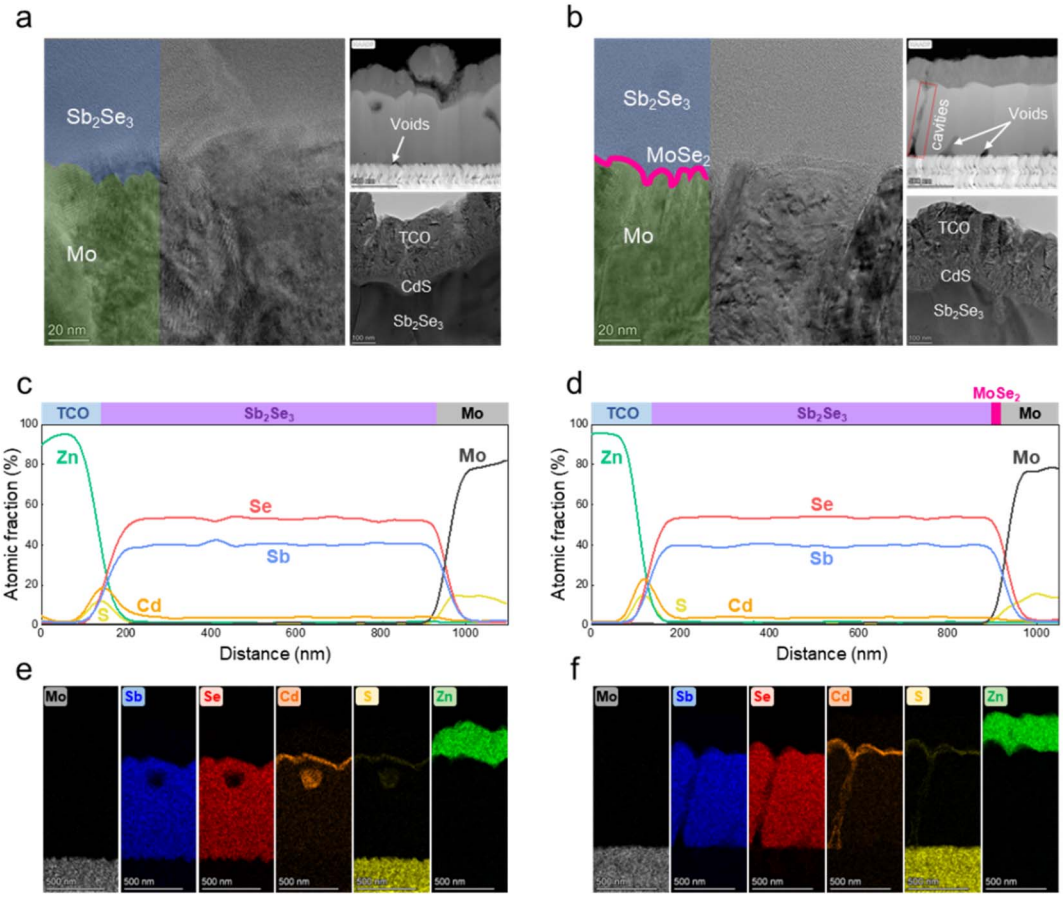

Fig. 2 Cross-sectional transmission electron microscopy (TEM) and high-angle annular dark-field (HAADF) scanning TEM (STEM) images of the back Mo/Sb_2Se_3 and front Sb_2Se_3/CdS interfaces of Sb_2Se_3 solar cell devices using (a) A(Mo) and (b) B($MoSe_2$). Energy dispersive spectroscopy (EDS) line scans of elemental distributions across the devices (c) A(Mo) and (d) B($MoSe_2$). EDS mapping images of elements (Mo, Sb, Se, Cd, S, and Zn) for (e) A(Mo) and (f) B($MoSe_2$).

EDS line scan profiles and corresponding EDS mapping images of Sb_2Se_3 devices A(Mo) and B($MoSe_2$), respectively. The EDS elemental composition maps for B($MoSe_2$) reveal dark domains in the Sb and Se composition maps, extending from the front to the bottom of the Sb_2Se_3 absorber layer, indicating spaces between Sb_2Se_3 grain boundaries. While a uniform Sb_2Se_3 layer formed on the ultrathin $MoSe_2$ interlayer, distinct structural variations were observed at the grain boundaries of the absorber.

The morphological and electrical properties of the surfaces and interfaces of Sb_2Se_3 thin films deposited onto Mo-only and $MoSe_2$/Mo contacts were examined using Kelvin probe force microscopy (KPFM) and conductive atomic force microscopy (c-AFM) with an atomic force microscope (AFM) system.

The root mean square surface roughness values for the Sb_2Se_3 thin films obtained from AFM topography, were 37.31 nm and 153.33 nm for A(Mo) and B($MoSe_2$), respectively. The increased surface roughness of the film with the $MoSe_2$ interlayer is attributed to the facile growth of Sb_2Se_3 with a preferred (*hk*1) orientation.[10]

The effect of this modified dominant crystal orientation on band bending properties at GBs was investigated. For this, the V_{CPD} distribution on the Sb_2Se_3 surface was obtained using KPFM (Fig. 3a–d). The resulting V_{CPD} values were converted to surface potential by calculating the sample work function using the following equation:[21]

$$V_{CPD} = \frac{\Delta\Phi}{e} = \frac{\Phi_{tip} - \Phi_{sample}}{e}, \quad (2)$$

where Φ_{tip} and Φ_{sample} denote the work functions of the tip and sample, respectively. Here, Φ_{tip} was determined by measuring the V_{CPD} value of a highly oriented pyrolytic graphite reference sample with a known work function of 4.60 eV. The potential difference between GBs and IGs can be represented by the variation in V_{CPD} at the GBs, expressed as: $\Delta V_{CPD,GBs} = V_{CPD}$ at IGs ($V_{CPD,IGs}$) − V_{CPD} at GBs ($V_{CPD,GBs}$). The statistical distribution of $\Delta V_{CPD,GBs}$ is presented in Fig. 3e. The displayed values were extracted from line profile data obtained across 40 GBs in three different map images, each measured at distinct locations on each sample. Following the incorporation of the $MoSe_2$ interlayer, the average $\Delta V_{CPD,GBs}$ increased from 32.1 mV to 42.0 mV, accompanied by a reduction in the number of GBs and IGs with low potential differences. Potential variation at GBs is significant as it promotes electron–hole separation and influences charge carrier recombination properties.[22]

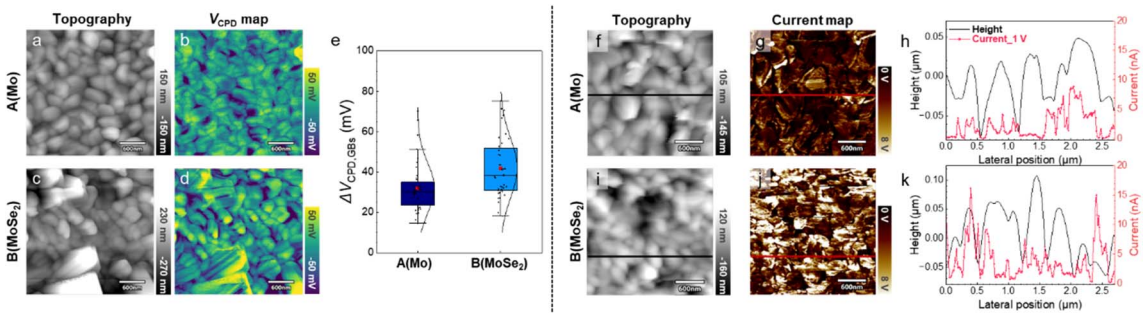

Fig. 3 Band bending at grain boundaries (GBs) and vertical current flow in Sb_2Se_3 thin films grown on different back-contact layers. Mapping images of (a and c) morphology and (b and d) contact potential difference (V_{CPD}) distribution on the Sb_2Se_3 surface for A(Mo) and B($MoSe_2$), respectively. (e) Statistical distribution of the potential difference between GBs and intra-grains (IGs), with the red dot on the box plot indicating the mean value of all measured data. Mapping images of (f and i) morphology and, (g and j) current flow measured at the Sb_2Se_3 surface, and (h and k) line profiles extracted along the marked line for A(Mo) and B($MoSe_2$), respectively.

Fig. S2a and b (ESI†) present the band bending diagrams of A(Mo) and B($MoSe_2$). Based on these, charge carrier dynamics at the GBs were examined. Upward band bending was observed in both samples, indicating the formation of an electron barrier at the GBs that repels electrons and attracts holes.[23] Generally, a higher potential barrier leads to more efficient charge carrier separation and reduces the number of trap states at GBs, which can degrade device performance. Overall, the enhanced band bending observed in the Sb_2Se_3 films deposited on the $MoSe_2$/Mo contact compared to those deposited on the Mo-only contact is anticipated to suppress electron–hole recombination and facilitate charge extraction.

The local current flow within the Sb_2Se_3 thin films was investigated using c-AFM. Current maps along the grain structure were obtained under a +1 V bias voltage, and representative line profiles were extracted along the marked lines on the map images (Fig. 3f–k). For both A(Mo) and B($MoSe_2$), current predominantly flowed through IGs rather than GBs. Compared to the Sb_2Se_3 thin film without the $MoSe_2$ interlayer, the overall conductivity of the film with the interlayer increased significantly. Quantitatively, the average current flow increased by 2.2 nA, from 2.1 nA to 4.3 nA, as calculated from measured current statistics.

In Sb_2Se_3 with a one-dimensional ribbon structure, charge carrier transport along the (*hk*1) orientation is more favorable than that along the (*hk*0) orientation. The controlled crystal orientation within the Sb_2Se_3 thin film achieved by introducing the $MoSe_2$ interlayer may explain the increased vertical current flow.[24] Additionally, improved back-contact band alignment could contribute to charge transport by effectively preventing electron leakage and facilitating hole extraction at the back interface.[25] Further details about the band structure will be discussed later. Overall, the enhanced charge carrier extraction and transport properties of B($MoSe_2$) are anticipated to improve device performance by increasing the short-circuit current (J_{SC}) and open-circuit voltage (V_{OC}).

To investigate charge transport properties at the interface and examine interfacial band alignment, the solar cell devices were mechanically dimpled using a dimple grinder to expose their interface laterally.[17] Schematic cross-sectional illustrations of the dimpled devices are presented in Fig. 4a and b. The boxed area indicates the focus of further analysis, with the optical microscopy images of this region displayed in Fig. 4c and d. Micro-Raman scattering spectra were obtained across the interface between the Sb_2Se_3 and Mo layers at the numbered spots in the optical images using a 532 nm wavelength laser (Fig. 4e and f). The laser power was carefully adjusted to prevent sample damage. At points 1 to 7, two distinct peaks at 190 cm^{-1} and 209 cm^{-1} appeared in both samples. These peaks, corresponding to the A_{1g} mode and Sb–Se vibrational mode, are representative peaks of Sb_2Se_3.[20,26] No significant peak shifts were observed between the two samples with different back-contact structures, indicating uniform polishing conditions. A phase change observed at point 8 confirmed the position of the back interface. At this point, A(Mo) displayed direct contact between Sb_2Se_3 and Mo. Conversely, in B($MoSe_2$), a peak around 240 cm^{-1} was observed, indicating that the thin $MoSe_2$ layer positioned between the Sb_2Se_3 and Mo layers was well exposed through grinding.[27]

The topographies and V_{CPD} distributions of the Sb_2Se_3/Mo and Sb_2Se_3/$MoSe_2$ interfaces were obtained using KPFM (Fig. 4g, h, k, and l). Notably, a significant change in the V_{CPD} difference between Sb_2Se_3 and the adjacent layer was observed, implying considerable modification of the interfacial band alignment. A detailed analysis of band bending at the interface was conducted using potential profiles extracted along the marked line on the topography and V_{CPD} map images (Fig. 4i and m). The V_{CPD} values were converted into surface potentials using eqn (1), as previously described. The potential variation at the interface increased from 70 mV to 123 mV with the introduction of $MoSe_2$. This altered band alignment directly impacted charge carrier transport. Schematic band diagrams of the interface, shown in Fig. 4j and n, illustrate these effects. At the Sb_2Se_3/Mo interface, a relatively weak ohmic contact formed, which poorly supported the flow of electrons and holes along the desired direction.[28] In contrast, the insertion of $MoSe_2$ at the back interface created an electron barrier that effectively blocked electron flow across the junction while promoting hole transport.[29] The improved back-contact quality suppressed carrier recombination and enhanced carrier diffusion at the

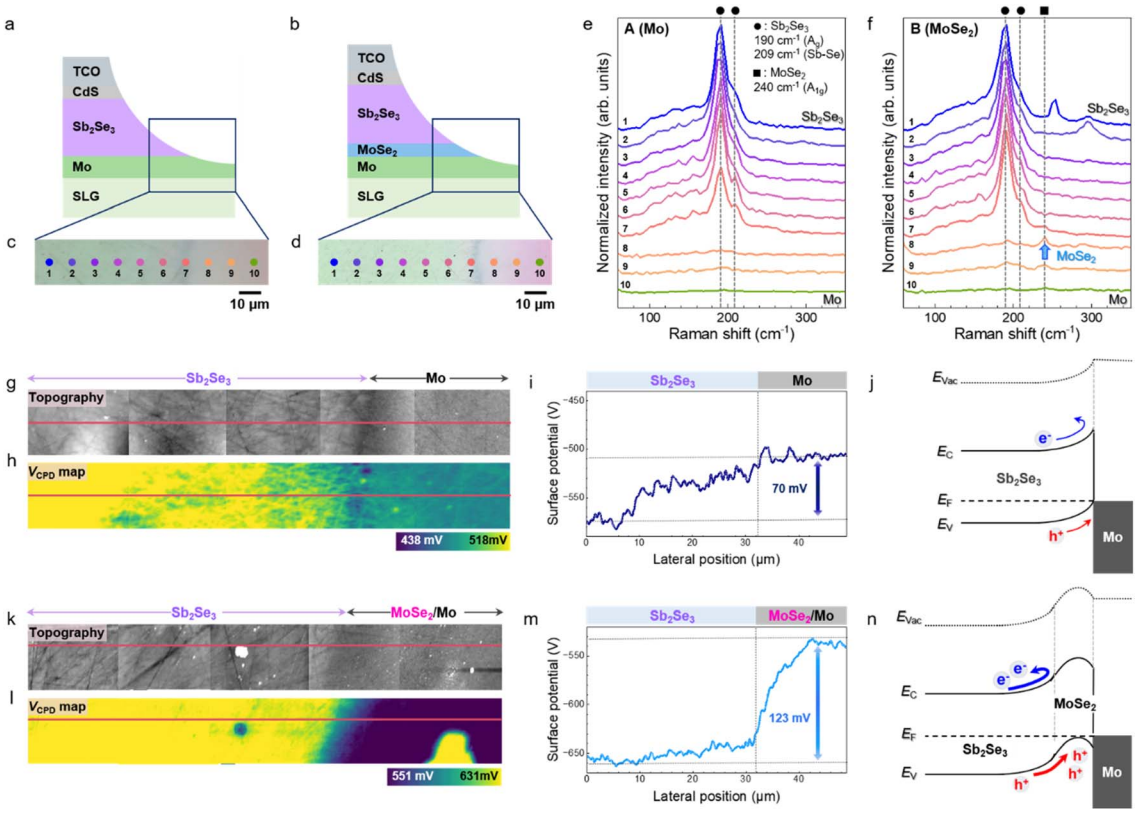

Fig. 4 Adjustment of the Sb_2Se_3/back-contact interface band alignment achieved by inserting the $MoSe_2$ interlayer, as examined using mechanically dimpled solar cell devices. (a and b) Cross-sectional illustrations of dimple-ground devices and (c and d) optical microscopy images of the exposed interfaces of A(Mo) and B($MoSe_2$), respectively. (e and f) Raman spectra measured at marked points along the Sb_2Se_3/back-contact interface, with assigned Raman peaks for the Sb_2Se_3 and $MoSe_2$ phases indicated using black circles and squares, respectively. Mapping images of (g and k) morphology and (h and l) V_{CPD} distribution at the Sb_2Se_3/back-contact interface for A(Mo) and B($MoSe_2$), respectively. (i and m) Surface potential profiles extracted along the marked line in the V_{CPD} map image. (j and n) Sb_2Se_3/back-contact interface band alignment and charge carrier (e^- and h^+) transport properties with and without the $MoSe_2$ interlayer, constructed based on the KPFM results.

junction, benefiting charge carrier transport and contributing to an increase in open-circuit voltage (V_{OC}).[24]

Fig. 5a–f illustrate the performance of Sb_2Se_3 solar cells with and without the $MoSe_2$ interlayer. The evaluated parameters include (a) open-circuit voltage (V_{OC}), (b) short-circuit current density (J_{SC}), (c) fill factor (FF), (d) power conversion efficiency, (e) shunt resistance (R_{sh}), and (f) series resistance (R_s) under AM 1.5G illumination. The device parameters of the solar cell devices without selenization treatment were compared to the device parameters of those subjected to 20-min selenization. Although the Jsc of the solar cells indicates minimal statistical influence from the $MoSe_2$ interlayer, this interlayer improves the photovoltaic performance, particularly in terms of V_{OC} and FF. Specifically, Sb_2Se_3 solar cells with the $MoSe_2$ interlayer exhibit higher average values and reduced FF variation compared to those without treatment. The R_{sh} value of the devices comprising the $MoSe_2$ interlayer was an order of magnitude higher than that of the device without $MoSe_2$, while R_s decreased (Fig. 5c and d). This trend is attributed to reduced current losses and minimized trap states in the films.[30] The current density–voltage (J–V) curves of the optimal device are illustrated in Fig. 5g, and the photovoltaic parameters are listed in Table 1. The control device with an Mo substrate achieves a maximum power conversion efficiency (PCE) of 2.835%, with corresponding V_{OC}, J_{SC}, and FF values of 0.360 V, 22.301 mA cm^{-2}, and 35.236%, respectively. Remarkably, the device with the $MoSe_2$ interlayer achieves an enhanced PCE of 5.538%, with V_{OC}, J_{SC}, and FF values of 0.426 V, 24.667 mA cm^{-2}, and 52.698%, respectively. Additionally, the EQE analysis (Fig. S3a†) shows better spectral responses at longer wavelengths (700 to 900 nm) using $MoSe_2$, indicating reduced Shockley–Read–Hall recombination and longer carrier lifetime. The overall improvement in EQE response is attributed to enhanced light absorption and charge carrier transport facilitated by the vertically oriented ($hk1$) nanorod structure of Sb_2Se_3. Despite the significant increases in V_{OC} and FF, we observed a slight increase in J_{SC}, mainly due to the unchanged absorber layer bandgap (Fig. S3b†). This enhancement is attributed to improved carrier transport, as illustrated schematically in Fig. 5h and i, for the Mo- and Mo/$MoSe_2$-based devices. The facilitated carrier flow, attributed to the ($hk1$)-preferred orientation of the Sb_2Se_3 absorber layer on the $MoSe_2$ interlayer, contributes to increased J_{SC}. Additionally, the quasi-ohmic contact formation between the Sb_2Se_3 absorber layer and $MoSe_2$ interlayer significantly improves V_{OC} and FF.

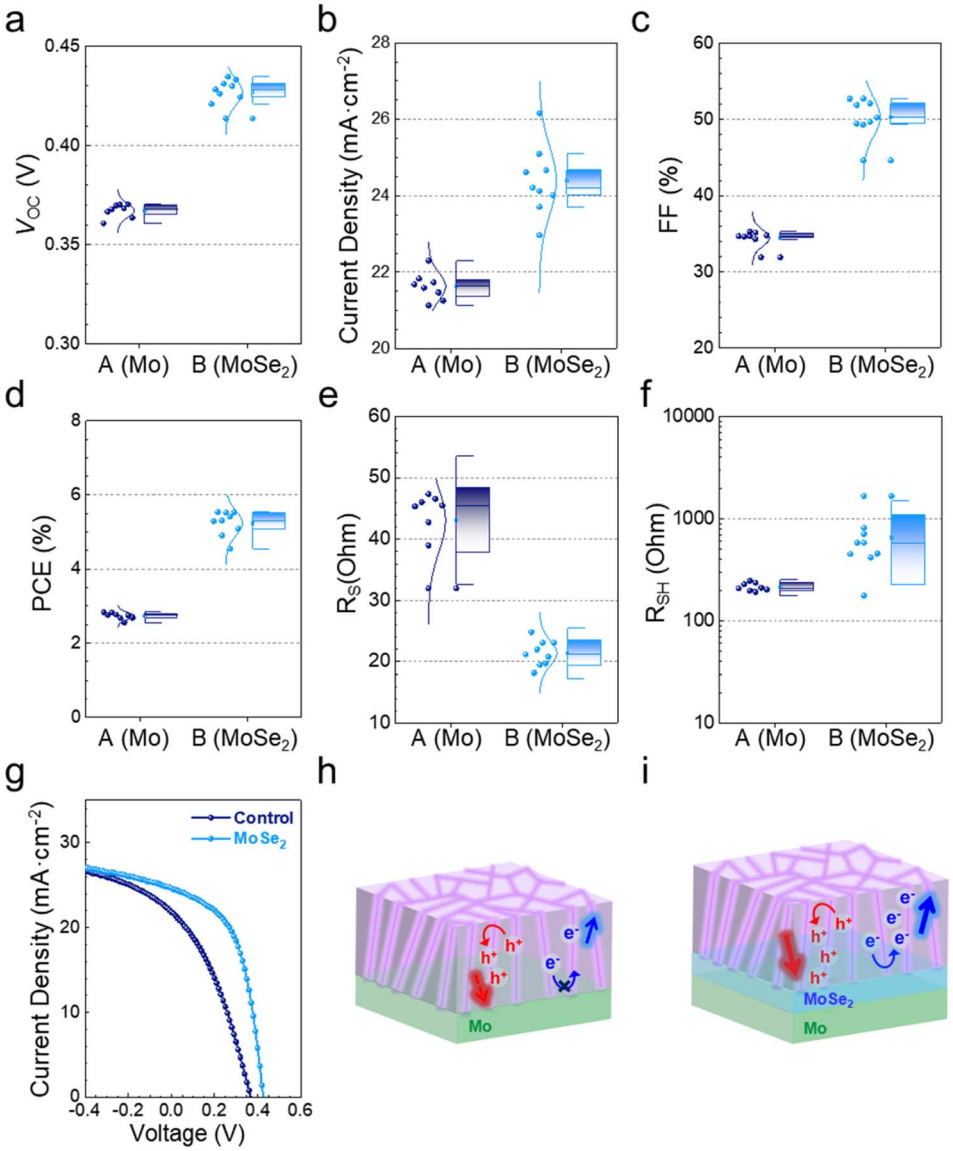

Fig. 5 (a–f) Statistical box plots of the solar cell parameters of the devices. (g) Current density–voltage curves of the devices under the standard AM 1.5G solar spectrum. Schematic illustrations of the modified charge transport mechanisms in devices with the (h) Mo substrate and (i) Mo/$MoSe_2$ substrate.

Table 1 Photovoltaic parameters of Sb_2Se_3 solar cells with and without $MoSe_2$, measured under one Sun AM 1.5G illumination

Samples	V_{OC} [V] (average)	J_{SC} [mA cm^{-2}] (average)	FF [%] (average)	PCE [%] (average)
Control	0.36082 (0.36723)	22.3014 (21.6249)	35.2364 (34.4020)	2.835 (2.7316)
$MoSe_2$	0.42604 (0.42697)	24.6678 (24.3959)	52.6986 (50.3075)	5.538 (5.2405)

Conclusion

This study offers insights into the improved interfacial charge carrier transport and the resulting enhancement in Sb_2Se_3 solar cell performance achieved through the insertion of an $MoSe_2$ interlayer. The formation of $MoSe_2$ at the interface between Sb_2Se_3 and Mo promotes the vertical growth of Sb_2Se_3 with an ($hk1$) orientation, consistent with previous studies. This altered crystal growth enhances band bending at the GBs, reducing carrier recombination and promoting charge separation. Additionally, a substantial increase in surface current indicates efficient charge flow in the vertical direction. We demonstrate changes in interfacial band alignment at the back contact by measuring the electrical potential distribution at the interface. The potential variation at the back interface increased by 53 mV, suggesting that $MoSe_2$ effectively blocks electron transport

while facilitating hole extraction. Improved ohmic contact quality significantly elevates the V_{OC} and FF of the solar cells, enabling a PCE of 5.538%. These findings underscore the importance of fine-tuning of interfacial charge transport properties to achieve high-performance Sb_2Se_3 solar cells.

Data availability

The data supporting the findings of this study are available within the article and its ESI.†

Conflicts of interest

There are no conflicts of interest to declare.

Acknowledgements

This study was supported by the Basic Science Research Program of the National Research Foundation of Korea (NRF), funded by the Ministry of Education (NRF-2018R1A6A1A03025340) and the Ministry of Science and ICT (NRF-2022M3J1A1064229 and RS-2024-00355905). Additional financial support was provided by the Ministry of Trade, Industry and Energy (MOTIE) and the Korea Institute for Advancement of Technology (KIAT) through the International Cooperative R&D Program (No. P0024567), as well as by NRF grants funded by the Ministry of Science and ICT (No. 2023R1A2C1007386).

References

1 A. Mavlonov, T. Razykov, F. Raziq, J. Gan, J. Chantana, Y. Kawano, T. Nishimura, H. Wei, A. Zakutayev, T. Minemoto, X. Zu, S. Li and L. Qiao, *Sol. Energy*, 2020, **201**, 227–246.
2 Y. Zhou, L. Wang, S. Chen, S. Qin, X. Liu, J. Chen, D.-J. Xue, M. Luo, Y. Cao, Y. Cheng, E. H. Sargent and J. Tang, *Nat. Photonics*, 2015, **9**, 409–415.
3 A. Bosio, G. Foti, S. Pasini and D. Spoltore, *Energies*, 2023, 16.
4 R. A. Lomas-Zapata, A. W. Prior and B. G. Mendis, *Sol. Energy*, 2023, **264**, 112054.
5 S.-N. Park, S.-Y. Kim, S.-J. Lee, S.-J. Sung, K.-J. Yang, J.-K. Kang and D.-H. Kim, *J. Mater. Chem. A*, 2019, **7**, 25900–25907.
6 X. Jin, Y. Fang, T. Salim, M. Feng, Z. Yuan, S. Hadke, T. C. Sum and L. H. Wong, *Adv. Mater.*, 2021, **33**, e2104346.
7 C. Zhang, R. Jiang, Y. Zheng, Y. Li, Z. Cai, C. Ma, Y. Cheng, J. Chu and J. Tao, *Adv. Energy Mater.*, 2025, **15**(7), 2403352.
8 Z.-X. Chen, Y. Xiang, H.-J. Ma, Y. Lei, C.-H. Cheng, H. Huang and Y.-C. Han, *Opt. Mater.*, 2024, **152**, 115537.
9 S. Rijal, D. B. Li, R. A. Awni, C. Xiao, S. S. Bista, M. K. Jamarkattel, M. J. Heben, C. S. Jiang, M. Al-Jassim and Z. Song, *Adv. Funct. Mater.*, 2022, **32**, 2110032.
10 S.-N. Park, S.-Y. Kim, S.-J. Lee, S.-J. Sung, K.-J. Yang, J.-K. Kang and D.-H. Kim, *Mater. Adv.*, 2022, **3**, 978–985.
11 Z. Li, X. Liang, G. Li, H. Liu, H. Zhang, J. Guo, J. Chen, K. Shen, X. San and W. Yu, *Nat. Commun.*, 2019, **10**, 125.
12 G. Chen, Y. Luo, M. Abbas, M. Ishaq, Z. Zheng, S. Chen, Z. Su, X. Zhang, P. Fan and G. Liang, *Adv. Mater.*, 2024, **36**, 2308522.
13 R. Kumari, Mamta, A. K. Chaudhary and V. N. Singh, *Adv. Theory Simul.*, 2023, **6**(12), 2300322.
14 M. D. K. Jones, J. A. Dawson, S. Campbell, V. Barrioz, L. D. Whalley and Y. Qu, *Front. Chem.*, 2022, **10**, 920676.
15 H. Wang, D. Zhuang, M. Zhao, H. Tong, M. Jia, J. Han, Z. Wu and Q. Gong, *ACS Appl. Mater. Interfaces*, 2024, **16**, 56957–56966.
16 F. I. Za'abar, Y. Yusoff, H. Mohamed, S. F. Abdullah, A. W. Mahmood Zuhdi, N. Amin, P. Chelvanathan, M. S. Bahrudin, K. S. Rahman, N. A. Samsudin and W. S. Wan Abdullah, *Coatings*, 2021, **11**(8), 930.
17 G. Lim, H. K. Park, W. H. Kim, S.-H. Kim, K.-J. Yang, J.-K. Kang, D.-H. Kim and W. Jo, *J. Mater. Chem. A*, 2023, **11**, 25555–25562.
18 Z. Cai, B. Che, Y. Gu, P. Xiao, L. Wu, W. Liang, C. Zhu and T. Chen, *Adv. Mater.*, 2024, **36**, e2404826.
19 X. Chen, Y. Zhao, C. Li, X. Wang, P. Xiao, J. Gong, T. Chen, X. Xiao and J. Li, *Adv. Energy Mater.*, 2024, **14**(33), 2400441.
20 S. Li, H. Shen, J. Chen, Y. Jiang, L. Sun, A. Raza and Y. Xu, *J. Mater. Sci.: Mater. Electron.*, 2019, **30**, 19871–19879.
21 Y. S. Kim, H. Chung, S. Kwon, J. Kim and W. Jo, *Nano Converg.*, 2022, **9**, 43.
22 T. T. Nguyen, J. Kim, Y. S. Kim, B. P. Nguyen and W. Jo, *J. Mater. Chem. A*, 2023, **11**, 10254–10266.
23 S. Chen, Y. A. Ye, M. Ishaq, D. L. Ren, P. Luo, K. W. Wu, Y. J. Zeng, Z. H. Zheng, Z. H. Su and G. X. Liang, *Adv. Funct. Mater.*, 2024, **34**(40), 2403934.
24 X. Wen, Z. Lu, X. Yang, C. Chen, M. A. Washington, G. C. Wang, J. Tang, Q. Zhao and T. M. Lu, *ACS Appl. Mater. Interfaces*, 2023, **15**, 22251–22262.
25 S. S. Youn, J. Kim, J. Na, W. Jo and G. Y. Kim, *ACS Appl. Mater. Interfaces*, 2022, **14**, 48229–48239.
26 A. Shongalova, M. R. Correia, B. Vermang, J. M. V. Cunha, P. M. P. Salomé and P. A. Fernandes, *MRS Commun.*, 2018, **8**, 865–870.
27 P. A. Markeev, E. Najafidehaghani, Z. Gan, K. Sotthewes, A. George, A. Turchanin and M. P. de Jong, *J. Phys. Chem. C Nanomater. Interfaces*, 2021, **125**, 13551–13559.
28 A. Sylla, N. G. A. Ignace, T. Siaka and J.-P. Vilcot, *OJMSi*, 2021, **09**, 339–350.
29 H. Deng, Y. Cheng, Z. Chen, X. Lin, J. Wu, Q. Zheng, C. Zhang and S. Cheng, *Adv. Funct. Mater.*, 2023, **33**(12), 2212627.
30 B. Qi and J. Wang, *Phys. Chem. Chem. Phys.*, 2013, **15**, 8972–8982.